High-pressure phase transformations in CaH_2

2008 J. Phys.: Condens. Matter 20 045211

(http://iopscience.iop.org/0953-8984/20/4/045211)

J. Phys.: Condens. Matter **20** (2008) 045211 (8pp) doi:10.1088/0953-8984/20/04/045211

High-pressure phase transformations in CaH_2

Yinwei Li[1], Bing Li[1], Tian Cui[1], Yan Li[1], Lijun Zhang[1], Yanming Ma[1,2,3] and Guangtian Zou[1]

[1] National Laboratory of Superhard Materials, Jilin University, Changchun 130012, People's Republic of China
[2] Laboratory of Crystallography, Department of Materials, ETH Zurich, Wolfgang-Pauli-Strasse10, CH-8093 Zurich, Switzerland

E-mail: mym@jlu.edu.cn

Received 25 October 2007
Published 8 January 2008
Online at stacks.iop.org/JPhysCM/20/045211

Abstract

The structural stabilities, lattice dynamics and electronic properties of CaH_2 under high pressures were studied using the density functional linear response theory. The calculations showed that CaH_2 transforms from the $PbCl_2$-type ($Pnma$) to the $InNi_2$-type ($P6_3/mmc$) structure at ~16 GPa in agreement with experiment. The theoretical and experimental Raman investigations demonstrated the occurrence of a high frequency E_{2g} mode of the $P6_3/mmc$ phase and explained why this mode was not observed in previous Raman experiments, in conflict with the proposed $P6_3/mmc$ symmetry of the phase structure. The calculations of the phonon dispersion curves revealed the dynamical instability of the $P6_3/mmc$ phase at pressures below 10 GPa caused by a soft transverse acoustic phonon mode at the zone boundary M point. The $P6_3/mmc$ phase was predicted to be an insulator and to transform to a metallic phase with an AlB_2-type structure ($P6/mmm$) at ~138 GPa. According to the electron–phonon coupling calculation, the superconducting temperature of the $P6/mmm$ CaH_2 phase cannot be higher than 1 mK. The charge transfers in the $Pnma$, $P6_3/mmc$, and $P6/mmm$ phases were also calculated and discussed.

(Some figures in this article are in colour only in the electronic version)

1. Introduction

Calcium hydride, CaH_2, is of considerable scientific and technological interest. It is applied in chemistry as a catalyst, condensation agent and desiccant. Recently, CaH_2 has attracted close attention as a hydrogen-storage material owing to its high hydrogen-to-metal ratio.

Under ambient conditions, CaH_2 crystallizes in the $PbCl_2$-type structure ($Pnma$, $Z = 4$) [1–4], in which Ca and two inequivalent H (labeled as H1 and H2 in figure 1(a)) atoms occupy Wyckoff 4c sites [1, 4]. The vibrational density of states (DOS) spectrum and phonon spectra of CaH_2 at ambient conditions have been measured by neutron vibrational spectroscopy [1, 5]. The vibrational modes of CaH_2 at ambient pressure have been assigned by lattice dynamics calculation using density functional theory (DFT) [1, 6]. The high pressure behavior of CaH_2 remained open until, recently, two independent Raman measurements [6, 7] revealed a pressure-induced structural phase transition at ~15 GPa. Tse *et al* [7] also performed a high pressure *in situ* x-ray diffraction (XRD) measurement. Combining the first-principles structural optimizations with the XRD, they suggested that the new high pressure phase should take the $InNi_2$-type structure ($P6_3/mmc$, $Z = 2$). However, XRD measurement fails to locate the exact positions of hydrogen. In the two experimental Raman measurements [6, 7], only one Raman mode was observed for this phase; therefore, more evidence is needed to validate the $P6_3/mmc$ structure of the new high pressure phase because from the group theory the $P6_3/mmc$ CaH_2 should possess two Raman active modes. Moreover, the metallization of the hydrogen-rich CaH_2 under high pressure is of great interest in pursuing the superconductor with a high transition temperature.

In view of the recent powder x-ray diffraction experiments on BaH_2, a sequence of phase transitions $Pnma \rightarrow P6_3/mmc$ (~2.5 GPa) $\rightarrow$ $P6/mmm$ (~50 GPa) was

[3] Author to whom any correspondence should be addressed.

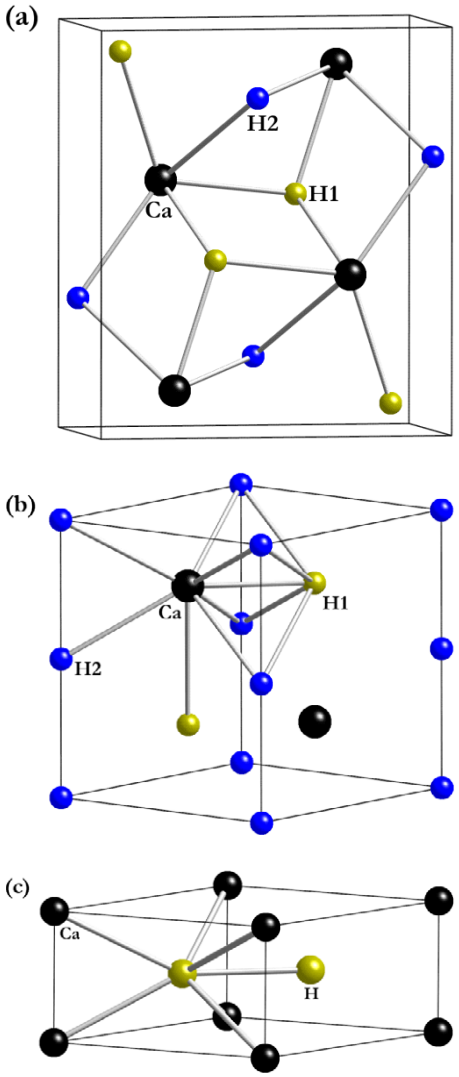

Figure 1. The crystal structures of CaH_2 for the $Pnma$ phase (No 62, $Z = 4$) at ambient pressure (a), $P6_3/mmc$ phase (No 194, $Z = 2$) at 18 GPa (b), and $P6/mmm$ phase (No 191, $Z = 1$) at 140 GPa (c).

adopted [8]. This motivated an investigation of the $P6/mmm$ structure for CaH_2, which is a chemical analog of BaH_2.

Here, we present a detailed theoretical study on the total energies, electronic band structure, and lattice dynamics of CaH_2 within the $Pnma$, the $P6_3/mmc$, and the $P6/mmm$ phases by means of *ab initio* calculations based on the density functional theory. A Raman measurement is also performed to identify the high frequency E_{2g} mode of the $P6_3/mmc$ phase. The experimental and theoretical joint study supports the validity of the $P6_3/mmc$ structure of the new high pressure phase. Moreover, a further pressure-induced phase transition of the $P6_3/mmc$ to the $P6/mmm$ is predicted to occur at 138 GPa. Importantly, the metallization of CaH_2 was achieved at the transformation to the $P6/mmm$ phase.

2. Computational details

The *ab initio* calculations were performed using the plane-wave pseudopotential method within the linear response density functional theory through the Quantum-ESPRESSO package [9]. We choose the generalized gradient approximation (GGA) for the exchange–correlation potential within the Perdew–Burke–Ernzerhof (PBE) parametrization [10]. The Troullier–Martins [11] norm-conserving scheme is employed to generate the tight pseudopotentials for Ca and H atoms, respectively, suitable for the high pressure study. The choices of the kinetic energy cutoffs of 120 Ryd for all phases, and $3 \times 6 \times 3, 9 \times 9 \times 6$, and $4 \times 4 \times 4$ k meshes for the $Pnma$, the $P6_3/mmc$, and the $P6/mmm$ phases, respectively, in the electronic integration of the first Brillouin zone (BZ) are found to be good enough for the total energy to converge within 0.01 mRyd/cell. The q meshes in the first BZ of $2 \times 4 \times 2$ for the $Pnma$, $4 \times 4 \times 3$ for the $P6_3/mmc$, and $4 \times 4 \times 4$ for the $P6/mmm$ structures were adopted in the calculation of the phonon dispersion curves. The Mulliken charge transfer calculations were carried out with the CASTEP code [12]. The electron–phonon coupling (EPC) of CaH_2 at high pressure is studied within the rigid-muffin-tin approximation (RMTA) [13, 14]. Raman intensities are computed from the second-order derivative of the electronic density matrix with respect to a uniform electric field [15].

Table 1. The theoretical lattice parameters of CaH_2 for the $Pnma$ structure at ambient pressure. The experimental data from [1, 4] and the previous theoretical results from [7] are also listed for comparison. V_0 is the unit cell volume.

	Present (0 K)	Expt[a] (9 K)	Expt[b] (293 K)	Theor.[c] (0 K)
a (Å)	5.9673	5.928 52(5)	5.925(1)	5.881
b (Å)	3.6062	3.577 74(3)	3.581(1)	3.559
c (Å)	6.8384	6.789 56(6)	6.776(1)	6.751
V_0 (Å^3)	147.156	144.011(1)	143.769	141.302
Ca (x)	0.2400	0.2387(1)	0.2378(1)	0.2394
Ca (z)	0.1099	0.1102(1)	0.1071(1)	0.1104
H1 (x)	0.3557	0.3558(1) ($D_1(x)$)	0.3573(6) ($D_1(x)$)	0.3556
H1 (z)	0.4265	0.4276(1) ($D_1(z)$)	0.4269(7) ($D_1(z)$)	0.4276
H2 (x)	0.9754	0.9750(1) ($D_2(x)$)	0.9739(6) ($D_2(x)$)	0.9742
H2 (z)	0.6765	0.6756(1) ($D_2(z)$)	0.6766(5) ($D_2(z)$)	0.6770

[a] Reference [1].
[b] Reference [4].
[c] Reference [7].

3. Results and discussion

3.1. Structural stabilities in CaH_2

The cell parameters and atomic positions for the $Pnma$, $P6_3/mmc$, and $P6/mmm$ structures were fully optimized at selected pressures. The calculated structural parameters for the $Pnma$ phase at ambient pressure are listed in table 1. The lattice parameters for the $P6_3/mmc$ structure at 18 GPa are optimized to be $a = 3.6340$ Å and $c = 4.7620$ Å. The Ca, H1, and H2 atoms occupy Wyckoff 2c, 2d, and 2a positions, respectively. For the $P6/mmm$ phase at 140 GPa, the lattice

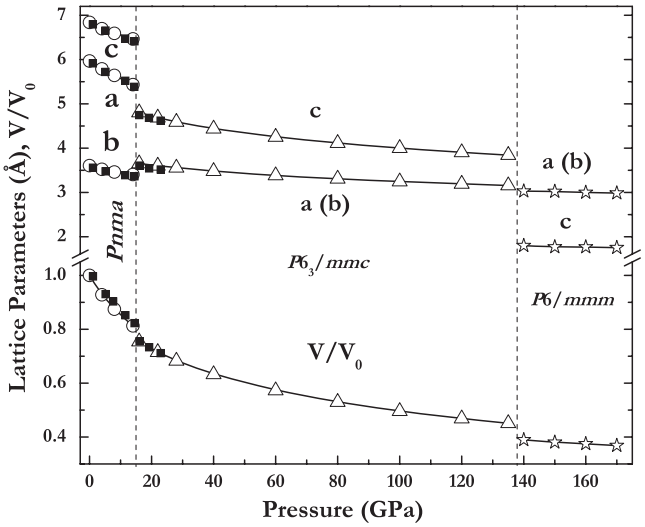

Figure 2. The calculated pressure dependences of the lattice parameters (a, b, c) and relative unit cell volume (V/V_0) of the $Pnma$ (open circles), $P6_3/mmc$ (open triangles) and $P6/mmm$ (open asterisks) phases of CaH_2 at 0 K. The experimental data (room temperature) taken from [7] are also denoted by solid squares for comparison. Dashed vertical lines at 15 and 138 GPa represent the phase transitions of $Pnma \rightarrow P6_3/mmc$ and $P6_3/mmc \rightarrow P6/mmm$, respectively.

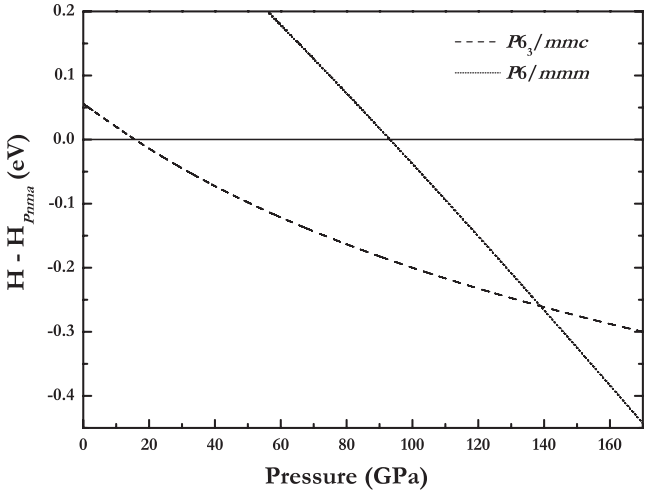

Figure 3. The calculated enthalpies for the $P6_3/mmc$ and $P6/mmm$ phases of CaH_2 relative to that of the $Pnma$ phase as functions of pressure.

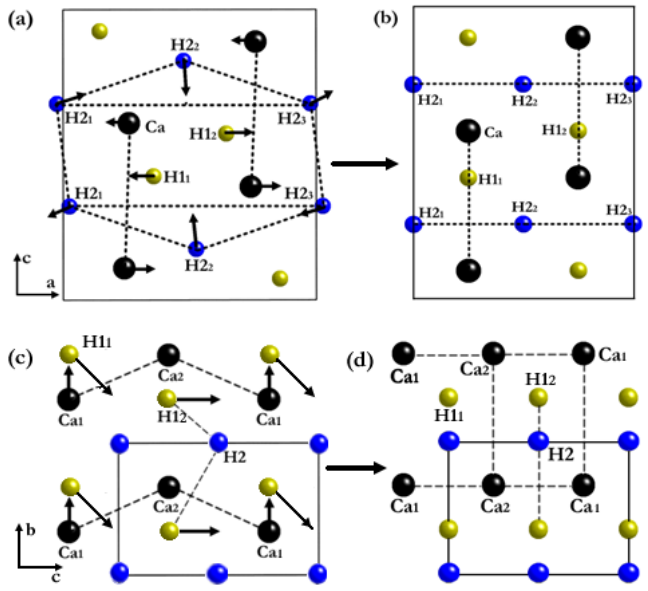

Figure 4. Projections of the orthorhombic $Pnma$ (a) and hexagonal $P6_3/mmc$ (b) (in the orthorhombic axes) structures onto the a–c plane. Projections of the hexagonal $P6_3/mmc$ (c) and hexagonal $P6/mmm$ (d) structures along the a-axis. The unit cells of all structures are outlined. The arrows in (a) and (c) represent the atomic displacements at the transition.

parameters are found to be $a = 3.03$ Å and $c = 1.80$ Å with Ca and H atoms sitting at 1a and 2d sites, respectively. Figure 1 represents schematic crystal structures of these three phases.

In table 1 the structural parameters of the $Pnma$ phase are compared with the available experimental data [1, 4] and earlier theoretical results [7]. It can be clearly seen that the calculated structural parameters are in excellent agreement with experiment within a maximum deviation of 0.9%. The slight overestimation of the theoretical lattice constants is typical of GGA. The pressure dependence of the lattice parameters and the relative unit cell volume together with the experimental results [7] for the three phases is presented in figure 2. The excellent agreement between the theory and experiment for the $Pnma$ and the $P6_3/mmc$ phases gives a strong support for the validity of the current theoretical model.

Our computational approach is based on constant-pressure static quantum mechanical calculations at $T = 0$ K, so the relative stability of different phases of CaH_2 can be deduced from the pressure dependence of the enthalpy instead of the Gibbs free energy [16]. As shown in figure 3, the calculation suggests that there exists a phase transition from the $Pnma$ to the $P6_3/mmc$ structure at 16 GPa that agrees well with the experimental transition pressure [6, 7]. The $P6/mmm$ structure becomes energetically more favorable above 138 GPa, indicating the existence of a second phase transition from the $P6_3/mmc$ to $P6/mmm$ structure. As seen from figure 2, the lattice parameters and the unit cell volumes abruptly change at the two phase transitions, implying a first-order nature of both phase transitions.

Since $P6_3/mmc$ is a supergroup of $Pnma$, in order to understand the mechanism of the $Pnma \rightarrow P6_3/mmc$ structural transition, the hexagonal $P6_3/mmc$ structure is described as the orthorhombic $Pnma$ structure with $a_o = c_h$, $b_o = a_h$, and $c_o = 3^{1/2}a_h$, and with the Ca, H1, and H2 atoms occupying the (1/4, 1/4, 1/12), (1/4, 1/4, 5/12), and (0, 3/4, 1/4) positions, respectively [17]. Projections of the two orthorhombic structures along the b-axis are shown in figures 4(a) and (b), respectively. The transformation from the $Pnma$ to $P6_3/mmc$ results in the atomic displacements along the arrows indicated in figure 4(a). The $H2_1$–$H2_2$–$H2_3$ angle increases after transformation and reaches 180° in the $P6_3/mmc$ structure as shown in figure 4(b). The transformation also involves a rotation of the coordination

Table 2. Frequencies of zone-center phonons for the *Pnma* phase at 0 GPa compared with the experimental data from [6] and previous theoretical results from [1]. The atomic vibrations for each mode are also listed.

Mode	Vibration type	ω (cm^{-1})	Mode	Vibration type	ω (cm^{-1})
Raman active			Infrared active		
B_{3g}	Ca/along *b* axis	137 (144[a] 139[b])	B_{1u}	Ca/along *a* axis	182 (183[a])
A_g	Ca/within *a*–*c* plane	147 (148[a] 149[b])	B_{3u}	Ca/along *c* axis	225 (220[a])
B_{1g}	Ca/along *b* axis	163 (171[a] 172[b])	B_{1u}	H2/within *a*–*c* plane	573 (577[a])
A_g	Ca/within *a*–*c* plane	190 (181[a] 193[b])	B_{3u}	H2/within *a*–*c* plane	579 (578[a])
B_{2g}	Ca/along *c* axis	223 (218[a] 223[b])	B_{2u}	H2/along *b* axis	596 (599[a])
B_{2g}	Ca/along *a* axis	262 (262[a])	B_{3u}	H1, H2/within *a*–*c* plane	701 (694[a])
B_{1g}	H2/along *b* axis	663 (663[a])	B_{1u}	H1, H2/within *a*–*c* plane	768 (747[a])
A_g	H2/within *a*–*c* plane	672 (673[a])	B_{3u}	H1, H2/within *a*–*c* plane	901 (880[a])
B_{3g}	H2/along *b* axis	695 (712[a] 692[b])	B_{2u}	H1/along *a* axis	986 (1007[a])
B_{2g}	H2/within *a*–*c* plane	715 (722[a])	B_{1u}	H1, H2/along *a* axis	995 (1000[a])
A_g	H1, H2/within *a*–*c* plane	754 (747[a] 749[b])	B_{1u}	H1/within *a*–*c* plane	1060 (1053[a])
B_{2g}	H2/within *a*–*c* plane	895 (872[a])	B_{3u}	H1, H2/along *a* axis	1141 (1127[a])
B_{2g}	H1/along *a* axis	976 (954[a])			
A_g	H1/along *b* axis	988 (974[a] 1002[b])	Silent		
B_{3g}	H1/along *b* axis	1022 (1038[a] 1018[b])	A_u	Ca/along *b* axis	115 (123[a])
B_{1g}	H1, H2/along *b* axis	1032 (1031[a])	A_u	H2/along *b* axis	618 (635[a])
A_g	H1/along *c* axis	1035 (1020[a] 1038[b])	A_u	H1/along *b* axis	957 (969[a])
B_{2g}	H1, H2/along *c* axis	1090 (1100[a] 1087[b])			

[a] Reference [1].
[b] Reference [6].

polyhedrons of Ca atoms about the *b*-axis. Projections of the hexagonal $P6_3/mmc$ and $P6/mmm$ structures along the *a*-axis are presented in figures 4(c) and (d), respectively, in order to illustrate the mechanism of the $P6_3/mmc \rightarrow P6/mmm$ transition. The formation of the $P6/mmm$ structure can be associated with the atomic displacements along the arrows in the $P6_3/mmc$ structure shown in figure 4(c). The Ca1 atoms move within the hexagonal layers while the H1 ($H1_1$ and $H1_2$) atoms are squeezed out of the layers. Note that these atomic movements result in an increased Ca1–Ca2–Ca3 angle. The $P6/mmm$ structure is formed when the angle reaches 180° as shown in figure 4(d).

3.2. *Lattice dynamical properties of CaH_2*

The phonons give a criterion for the crystal stability and indicate, through soft modes, possible structural changes. If all phonon frequencies $\omega^2(\mathbf{k})$ are positive, the crystal is at least locally stable [18]. Thus, the phonon dispersion curves of the *Pnma*, $P6_3/mmc$, and $P6/mmm$ phases of CaH_2 were calculated within the linear response theory at selected pressures. The primitive cells of the *Pnma*, $P6_3/mmc$, and $P6/mmm$ CaH_2 contain four, two, and one formula units, leaving 36, 18, and 9 phonon branches, respectively. The calculated zone-center (Γ) phonon eigenvectors were used to deduce the symmetry labels of phonon modes. The group theory analysis shows that the 33 optic modes of the *Pnma* CaH_2 at the zone center have the irreducible representations

$$\Gamma_{Pnma} = 6A_g^R + 3A_u + 3B_{1g}^R + 6B_{2g}^R + 3B_{3g}^R + 5B_{1u}^{IR} + 2B_{2u}^{IR} + 5B_{3u}^{IR}.$$

The 15 $P6_3/mmc$ CaH_2 optic modes take the irreducible representations

$$\Gamma_{P63/mmc} = 2A_{2u}^{IR} + 2B_{2g} + B_{1u} + 2E_{2g}^R + 2E_{1u}^{IR} + E_{2u}.$$

For the $P6/mmm$ CaH_2, six optic modes have the irreducible representations

$$\Gamma_{P6/mmm} = A_{2u}^{IR} + B_{2g} + E_{2g}^R + E_{2u}^{IR}.$$

The symbols A and B represent non-degenerate vibrational modes, while E doubly degenerate modes. The Raman active modes are labeled by superscript R and infrared active by IR while the silent modes are unmarked. The calculated frequencies at the Γ point of the *Pnma* CaH_2 at 0 GPa along with the available experimental [6] and previous theoretical results [1] are listed in table 2, those of the $P6_3/mmc$ CaH_2 at 20.6 GPa and the $P6/mmm$ CaH_2 at 138 GPa in table 3. One can find that the agreement between the theory and experiments is excellent by the evidence of a maximum deviation of 5% in the low frequency mode B_{1g} (172 cm^{-1}). The atomic vibrations for every mode of the three phases are also listed in tables 2 and 3.

The calculated phonon dispersion curves and projected densities of states (PDOS) for the *Pnma* CaH_2 at different pressures are presented in figure 5. At 0 GPa, all phonon frequencies are positive in the whole BZ and the calculated PDOS agrees well with the available experiment [1] that only measured the high frequency vibrations of hydrogen. With increasing pressure to 18 GPa, all modes shift to higher frequencies, indicating that the *Pnma* CaH_2 is dynamically stable under high pressure. The dispersion curves are divided into two groups by a large gap (about 9.3 THz at 0 GPa). The

Table 3. Frequencies of zone-center phonons for the CaH_2 with the $P6_3/mmc$ phase at 20.6 GPa and the $P6/mmm$ phase at 138 GPa compared with the experimental data from [6].

$P6_3/mmc$			$P6/mmm$		
Mode	Vibration type	ω (cm^{-1})	Mode	Vibration type	ω (cm^{-1})
		Raman active			
E_{2g}	Ca/within a–b plane	212 (220[a])	E_{2g}	H/within a–b plane	1729
E_{2g}	H1/within a–b plane	1395			
		Infrared active			
A_{2u}	H1, H2/along c axis	725	A_{2u}	H/along c axis	1276
E_{1u}	H2/within a–b plane	865	E_{1u}	H/within a–b plane	1436
A_{2u}	H1/along c axis	924			
E_{1u}	H1/within a–b plane	1046			
		Silent			
B_{2g}	Ca/along c axis	306	B_{2g}	H/along c axis	1459
B_{2g}	H1, H2/along c axis	911			
E_{2u}	H2/within a–b plane	911			
B_{1u}	H2/along c axis	1074			

[a] Reference [6].

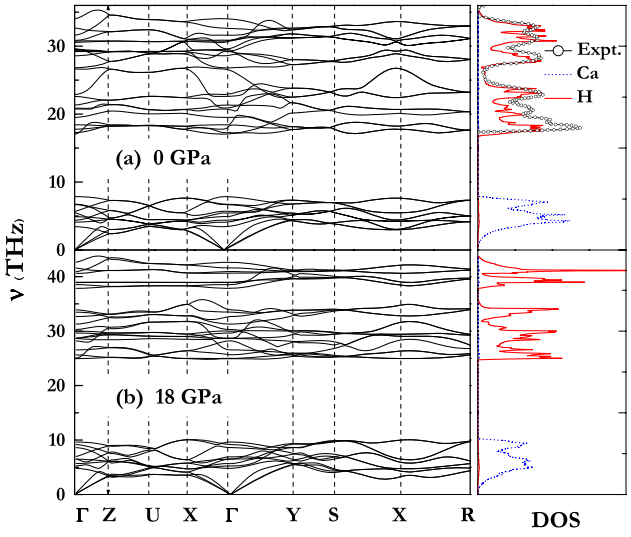

Figure 5. The calculated phonon dispersion curves and the vibrational projected phonon DOS of the $Pnma$ CaH_2 at 0 (a) and 18 GPa (b) along with the experimental data (open circles) from [1].

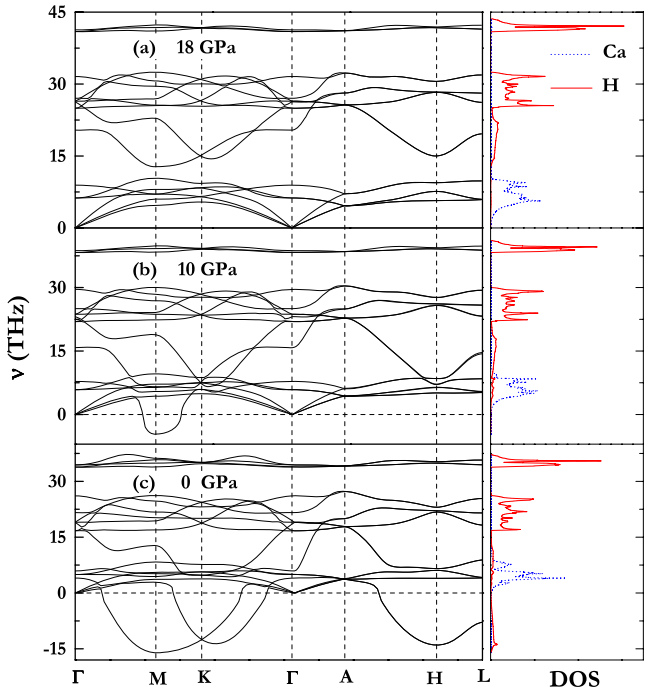

Figure 6. The calculated phonon dispersion curves and vibrational projected phonon DOS of the $P6_3/mmc$ CaH_2 at different pressures.

low frequency vibrations are dominated by Ca while the high frequency vibrations by H.

Figure 6 presents the computed phonon dispersion curves and PDOS of CaH_2 with the $P6_3/mmc$ structure at 0, 10, and 18 GPa. At 18 GPa, no imaginary phonon frequency is observed in the whole BZ, indicating that the $P6_3/mmc$ structure of CaH_2 is dynamically stable. At a lower pressure of 10 GPa, the phonon frequency of the transverse acoustic (TA) mode at the zone boundary point M (0, 0.5, 0) becomes imaginary, signaling a structural instability. More points with imaginary phonon frequencies appear at 0 GPa. The variation of the TA mode at the M point with decreasing pressure is presented in the main panel of figure 7. The estimated pressure for phonon softening to zero frequency is ∼10.5 GPa, which is about 5.5 GPa smaller than the calculated equilibrium pressure, ∼16 GPa, of the $Pnma \leftrightarrow P6_3/mmc$ transformation at $T = 0$ K. The squared frequencies υ^2 for the TA (M) mode with decreasing pressure are also plotted in inset (a) of figure 7 and a nearly perfect linear relation between υ^2 and the pressure is obtained. Such behavior is consistent with the Landau theory of pressure-induced soft mode phase transitions [19]. The schematic representation of eigenvectors for the soft TA phonon mode at the M point is shown in inset (b) of figure 7. The arrows represent the directions of the atomic vibrations. As evidenced by the calculated eigenvectors, all the Ca cations keep fixed, while the H1 and H2 anions vibrate parallel to

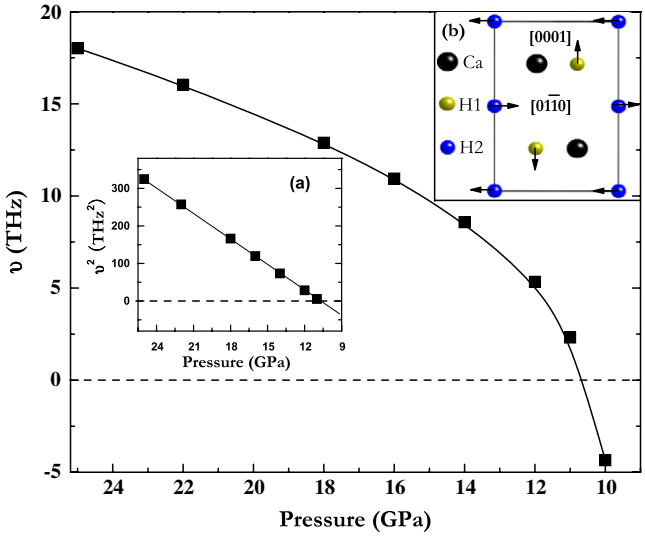

Figure 7. Main figure: calculated TA phonon frequencies at the M (0, 0.5, 0) point in the $P6_3/mmc$ CaH_2 as a function of pressure. Inset: (a) the calculated squared phonon frequencies ν^2 as a function of pressure. The solid line through the data points is the linear fit; (b) the eigenvector for the soft TA phonon mode at the M point. The arrows show the directions of atomic displacements.

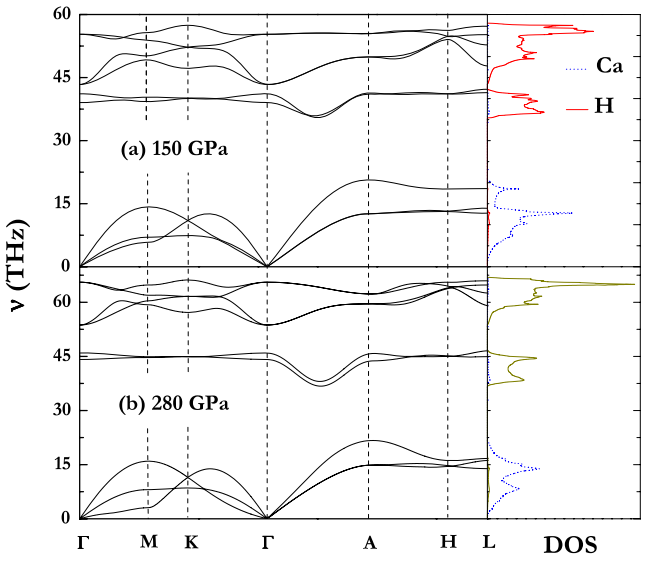

Figure 8. The calculated phonon dispersion curves and vibrational projected DOS of CaH_2 with the $P6/mmm$ structure at 150 GPa (a) and 280 GPa (b).

the [0001] and [01$\bar{1}$0] directions, respectively. Such atomic motions could break the symmetry of the system, and this is why the $P6_3/mmc$ structure becomes unstable and transforms to the $Pnma$ structure when the pressure is released.

In order to check the dynamical stability of the predicted $P6/mmm$ structure in CaH_2, we calculated its phonon dispersion curves and PDOS at high pressures as shown in figure 8. At 150 GPa, all phonon square frequencies proved to be positive in the whole BZ, indicating the dynamical stability of the $P6/mmm$ CaH_2. As the pressure increases, all modes shift to higher frequencies with the only exception for the

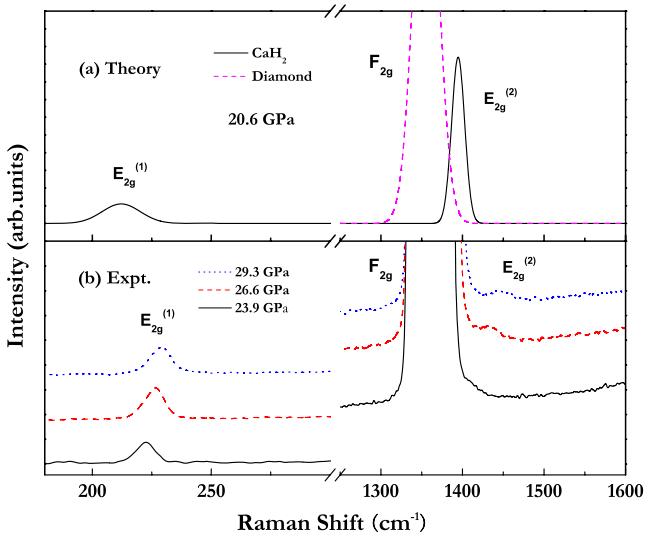

Figure 9. (a) The calculated Raman spectra of the $P6_3/mmc$ CaH_2 and diamond at 20.6 GPa; (b) the measured Raman spectra of CaH_2 and diamond anvils at different pressures.

lowest acoustic mode at the M (0, 0.5, 0) point that slightly softens with pressure. It is expected that this mode might soften to zero at a sufficiently high pressure. Nevertheless, the results show that the $P6/mmm$ CaH_2 will be dynamically stable up to 280 GPa.

3.3. *Raman spectra of the $P6_3/mmc$ phase of CaH_2*

Raman spectroscopy is routinely used as an experimental tool for the characterization of materials, and the theoretical determination of Raman spectra is a powerful complementary tool to the experimental analysis, particularly at extreme conditions of pressure and temperature [20].

For the $P6_3/mmc$ structure of CaH_2, the group theory analysis gives two Raman E_{2g} modes while only the low frequency mode was identified in the experiments [6, 7]. In order to examine if the high frequency E_{2g} mode is too weak to be observed, we calculated the Raman spectra of the $P6_3/mmc$ CaH_2 at 20.6 GPa. As shown in figure 9(a), the two calculated Raman peaks labeled as $E_{2g}^{(1)}$ and $E_{2g}^{(2)}$ are the low and high frequency modes, respectively. The $E_{2g}^{(2)}$ mode at 1395 cm^{-1} has stronger intensity than the $E_{2g}^{(1)}$ mode. The failure in the experimental observation of the $E_{2g}^{(2)}$ peak in earlier experiments could be attributed to its overlapping with the much stronger Raman peak F_{2g} (1355 cm^{-1} at 20.6 GPa) of diamond. Our Raman shift calculation indicates that the frequency difference between the F_{2g} and $E_{2g}^{(2)}$ modes increases from 40 cm^{-1} at 20.6 GPa to 65 cm^{-1} at 25 GPa. Therefore, we performed Raman measurements to identify the $E_{2g}^{(2)}$ mode at higher pressures than previously. The experimental technique has been described elsewhere [6]. The Raman spectra of CaH_2 at pressures of 23.9, 26.6, and 29.3 GPa are presented in figure 9(b). One can see that a weak Raman peak grows beside the F_{2g} peak and shifts to higher energies with increasing pressure. The peak position agrees well with our prediction for

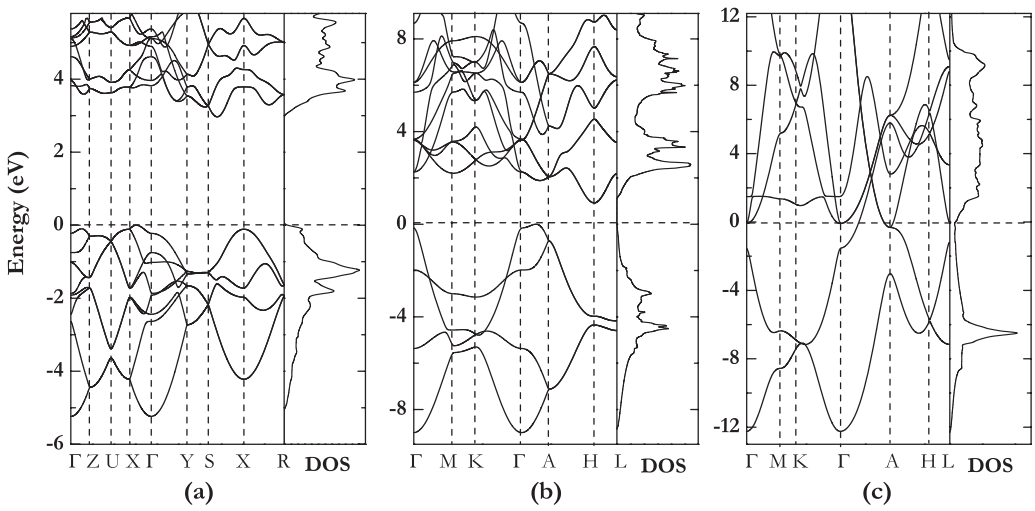

Figure 10. Electronic band structures of CaH_2 within the $Pnma$ phase at 0 GPa (a), the $P6_3/mmc$ phase at 40 GPa (b), and the $P6/mmm$ phase at 138 GPa (c). The horizontal dashed lines represent the Fermi level.

the $E_{2g}^{(2)}$ mode. However, the spectral intensity of the $E_{2g}^{(2)}$ mode in theory is much stronger than in experiment. Nevertheless, the occurrence of both experimental Raman peaks in the predicted $E_{2g}^{(1)}$ and $E_{2g}^{(2)}$ positions is convincing evidence that the high pressure phase of CaH_2 has the suggested $P6_3/mmc$ structure.

3.4. Electronic properties of CaH_2

The calculated electronic band structures and DOS for the three phases are presented in figure 10. It is found that the electronic bands of the $Pnma$ and $P6_3/mmc$ phases are separated by a minimum indirect gap of 2.97 eV at 0 GPa and 0.92 eV at 40 GPa, respectively, suggesting a non-metallic nature of both phases. The energy gap of the $P6_3/mmc$ phase increases slightly with pressure and reaches 1.11 eV at 120 GPa. Therefore, the metallic state is not feasible within the $P6_3/mmc$ structure. However, the metallization of CaH_2 is achieved in the $P6/mmm$ phase at 138 GPa by evidence of the band gap closure shown in figure 10(c). The calculated total DOS at the Fermi level is 0.1765 states/eV/f.u. at this pressure. The total DOS slightly increases with pressure up to 0.1811 states/eV/f.u. at 160 GPa.

The partial DOSs of CaH_2 at different pressures are plotted in figure 11. One can find that for the $Pnma$ structure at ambient pressure the valence bands mainly originate from two inequivalent H 1s states, indicating the covalent H–H bonding nature, while the contributions from the Ca 4s and 3d orbitals are quite small. The involvement of 3d electrons in the valence band is a reflection of hybridization of Ca 4s and 3d orbitals. The charge transfer from Ca 4s to H 1s results in a Ca–H ionic bonding behavior. Interestingly, the hybridization between Ca 4s and 3d orbitals becomes stronger with increasing pressure, causing a significant 3d contribution to the valence band as shown in figures 11(b) and (c). Particularly, for the $P6/mmm$ structure at 160 GPa, the bonding between Ca and H is more likely to be covalent (figure 11(c)). To further quantitatively understand the charge transfer behavior under pressure, the

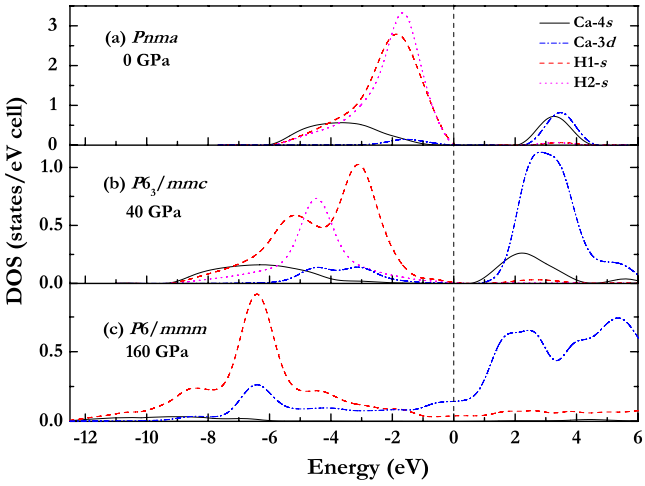

Figure 11. Calculated partial density of states of CaH_2 with the $Pnma$ structure at 0 GPa (a), the $P6_3mmc$ structure at 40 GPa (b), and the $P6/mmm$ structure at 160 GPa (c). The tops of the valence bands in the $Pnma$ and the $P6_3/mmc$ phases and the Fermi energy in the $P6/mmm$ phase were set to be zero.

Mulliken population analysis for the three phases is also performed. As shown in table 4, the charge transfers of Ca 4s $\rightarrow$ H 1s and Ca 4s $\rightarrow$ 3d are calculated to be 1.01e and 0.76e, respectively, at ambient pressure. With increasing pressure, both Ca 4s and H 1s electrons are readily transferred to Ca 3d, giving a net charge of 1.08e at 40 GPa and 1.90e at 160 GPa for Ca 3d. The electrons located at the Fermi level (figure 11(c)) for the $P6/mmm$ structure are mainly from Ca 3d. The pressure-induced Ca 4s $\rightarrow$ 3d and H 1s $\rightarrow$ Ca 3d charge transfers might be responsible for the phase transformations of $Pnma \rightarrow P6_3/mmc \rightarrow P6/mmm$.

3.5. Electron–phonon coupling in the $P6/mmm$ structure

The electron–phonon coupling of the $P6/mmm$ CaH_2 was studied within the RMTA [12, 13] at two different pressures.

Table 4. The calculated s and d electrons of each atom and the atomic Mulliken charges for the $Pnma$, the $P6_3/mmc$, and the $P6/mmm$ phases at 0, 40, and 160 GPa, respectively. Pseudo-atomic calculations performed here for Ca and H are $3s^2 3p^6 4s^2$ and $1s^1$, respectively.

Phase	Atom	s (e)	d (e)	Charge (e)
$Pnma$	Ca	2.23	0.76	1.01
(0 GPa)	H1	1.51		−0.51
	H2	1.50		0.50
$P6_3/mmc$	Ca	2.07	1.08	0.86
(40 GPa)	H1	1.45		−0.45
	H2	1.41		−0.41
$P6/mmm$	Ca	1.85	1.90	0.46
(160 GPa)	H1	1.23		−0.23
	H2	1.23		−0.23

Table 5. The calculated electronic DOS at the Fermi level, $N_{Ca}(E_F)$ and $N_H(E_F)$. The mean squares of the electron–phonon matrix element averaged over E_F for Ca ($\langle I^2\rangle_{Ca}$) and H ($\langle I^2\rangle_H$) using the RMTA. The square roots of the weighted mean square of the phonon frequency $\langle\omega^2\rangle^{1/2}$ from Ca and H contributions through the QUANTUM ESPRESSO code. The partial (λ_{Ca} and λ_H) and total (λ_{Total}) EPC parameters, and superconducting transition temperature (T_c) with the conventional choice of $\mu^* = 0.1$ at pressures of 150 and 280 GPa.

Pressure (GPa)	150	280
$N_{Ca}(E_F)$ (states/Ryd spin u.c.)	0.47	0.35
$N_H(E_F)$ (states/Ryd spin u.c.)	0.23	0.33
$\langle I^2\rangle_{Ca}$ (eV^2 Å^{-2})	23.32	35.45
$\langle I^2\rangle_H$ (eV^2 Å^{-2})	3.8	4.24
$\langle\omega^2\rangle_{Ca}^{1/2}$ (K)	539	544
$\langle\omega^2\rangle_H^{1/2}$ (K)	2224	2475
λ_{Ca}	0.1139	0.1343
λ_H	0.0873	0.0622
λ_{Total}	0.2012	0.1965
T_c (K)	1.0×10^{-3}	5×10^{-4}

The theory of the RMTA method has been described elsewhere [21]. As shown in table 5, the calculated mean squares of the electron–phonon matrix elements $\langle I^2\rangle_{Ca}$ and $\langle I^2\rangle_H$ significantly increase with pressure, that enhances the McMillan–Hopfield parameter $\eta_i = N(E_F)\langle I_i^2\rangle$ [22]. The mean squares of the phonon frequencies $\langle\omega^2\rangle_{Ca}$ and $\langle\omega^2\rangle_H$ increase with pressure, too, that decreases the T_c. As a result, the T_c calculated with the conventional choice of $\mu^* = 0.1$ reaches only 1.0×10^{-3} and 5×10^{-4} K at 150 and 280 GPa, respectively. We therefore conclude that the $P6/mmm$ CaH_2 is not a good candidate for the superconductor.

4. Conclusions

The *ab initio* total energy calculations have demonstrated that a first-order phase transition from the $PbCl_2$-type ($Pnma$) to the $InNi_2$-type structure ($P6_3/mmc$) in CaH_2 occurs at 16 GPa in good agreement with the available experimental data, and another first-order transition to the AlB_2-type structure ($P6/mmm$) takes place at 138 GPa. The evolution of the high energy E_{2g} mode in the $P6_3/mmc$ phase with increasing pressure was studied theoretically. The corresponding peak was then observed in the Raman experiment exactly at the predicted energy, thus illustrating the power of theoretical analysis. The $P6_3/mmc$ phase is found to be insulating with the indirect energy gap slightly increasing with pressure, while the $P6/mmm$ phase is metallic. The electron–phonon coupling calculation does not support the potential superconductivity within the $P6/mmm$ phase. The Mulliken population analysis reveals that the pressure-induced Ca 4s → 3d and H 1s → Ca 3d charge transfers might be responsible for the series of phase transformations $Pnma \rightarrow P6_3/mmc \rightarrow P6/mmm$.

Acknowledgments

The authors gratefully acknowledge the financial support of the NSAF of China (No 10676011), the China 973 Program (No 2005CB724400), the NDFCEM (No 20050183062), the SRF for ROCS, SEM, the Program for 2005 New Century Excellent Talents in University, and the 2006 Project for Scientific and Technical Development of Jilin Province.

References

[1] Wu H *et al* 2006 Structure and vibrational spectra of calcium hydride and deuteride *J. Alloys Compounds* **436** 51–5
[2] Zintl E and Harder A 1935 *Z. Elektrochem.* **43** 33
[3] Bergsma J and Loopstra B O 1962 *Acta Crystallogr.* **15** 92
[4] Andresen A F, Maeland A J and Slotfeldt-Ellingsen D 1977 *J. Solid State Chem.* **20** 93
[5] Maeland A J 1970 *J. Chem. Phys.* **52** 3952
[6] Li B, Li Y, Yang K, Cui Q, Ma Y and Zou G 2007 *J. Phys.: Condens. Matter* **19** 226205
[7] Tse J S, Klug D D, Desgreniers S, Smith J S, Flacau R, Liu Z, Hu J, Chen N and Jiang D T 2007 *Phys. Rev.* B **75** 134108
[8] Kinoshita K, Nishimura M, Akahama Y and Kawamura H 2007 *Solid State Commun.* **141** 69
[9] Baroni S *et al* http://www.pwscf.org
[10] Perdew J P and Burke K 1996 *Int. J. Quantum Chem.* **S 57** 309
[11] Troullier N and Martins J L 1991 *Phys. Rev.* B **43** 1993
[12] Segall M D, Lindan P J D, Probert M J, Pickard C J, Hasnip P J, Clark S J and Payne M C 2002 *J. Phys.: Condens. Matter* **14** 2717
[13] Gaspari G D and Gyorffy B L 1972 *Phys. Rev. Lett.* **28** 801
[14] Pickett W E 1982 *Phys. Rev.* B **25** 745
Papaconstantopoulos D A, Boyer L L, Klein B M, Williams A R, Morruzzi V L and Janak J F 1977 *Phys. Rev.* B **15** 4221
[15] Lazzeri M and Mauri F 2003 *Phys. Rev. Lett.* **90** 036401
[16] Catti M 2005 *Phys. Rev.* B **72** 064105
[17] Leger J M, Hainex J, Atouf A, Schulte O and Hull S 1995 *Phys. Rev.* B **52** 13247
[18] Lodziana Z, Parlinski K and Hafner J 2001 *Phys. Rev.* B **63** 134106
[19] Samara G A and Peercy P S 1981 *Solid State Physics* vol 36, ed H Ehrenreich, F Seitz and D Turnbull (New York: Academic)
[20] Liang Y, Miranda C R and Scandolo S 2006 *J. Chem. Phys.* **125** 194524
[21] Zhang L, Xie Y, Cui T, Li Y, He Z, Ma Y and Zou G 2006 *Phys. Rev.* B **74** 184519
[22] Hopfield J J 1969 *Phys. Rev.* **186** 443